POLITECNICO DI TORINO
Repository ISTITUZIONALE

Glass-ceramic joining of Fe22Cr porous alloy to Crofer22APU: interfacial issues and mechanical properties

Original
Glass-ceramic joining of Fe22Cr porous alloy to Crofer22APU: interfacial issues and mechanical properties / D'Isanto, F., Salvo, M., Molin, S., Koszelow, D., Javed, H., Akram, S., Chrysanthou, A., Smeacetto, F.. - In: CERAMICS INTERNATIONAL. - ISSN 0272-8842. - ELETTRONICO. - 48:19 part A(2022), pp. 28519-28527. [10.1016/j.ceramint.2022.06.166]

Availability:
This version is available at: 11583/2970727 since: 2022-08-24T14:46:08Z

Publisher:
Elsevier

Published
DOI:10.1016/j.ceramint.2022.06.166

Terms of use:

This article is made available under terms and conditions as specified in the corresponding bibliographic description in the repository

Publisher copyright
Elsevier postprint/Author's Accepted Manuscript

© 2022. This manuscript version is made available under the CC-BY-NC-ND 4.0 license http://creativecommons.org/licenses/by-nc-nd/4.0/.The final authenticated version is available online at: http://dx.doi.org/10.1016/j.ceramint.2022.06.166

(Article begins on next page)

02 November 2026

Revised Manuscript (Clean Version) Click here to view linked References

Glass-ceramic joining of Fe22Cr porous alloy to Crofer22APU: interfacial issues and mechanical properties

Fabiana D'Isanto[1]*, Milena Salvo[1], Sebastian Molin[2], Damian Koszelow[2], Hassan Javed[3], Sufyan Akram[4], Andreas Chrysanthou[4] and Federico Smeacetto[1].

[1] Department of Applied Science and Technology, Politecnico di Torino, Corso Duca degli Abruzzi 24, 10129, Turin, Italy.

[2] Advanced Materials Centre, Faculty of Electronics, Telecommunications and Informatics, Gdańsk University of Technology, ul. G. Narutowicza 11/12, 80-233 Gdańsk, Poland.

[3] Sunfire GmbH, Gasanstaltstraße 2, 01237, Dresden, Germany.

[4] School of Physics, Engineering and Computer Science, University of Hertfordshire, College Lane, Hatfield, Herts AL10 9AB, UK.

*Corresponding author.

E-mail address: fabiana.disanto@polito.it (F. D'Isanto)

Tel +39 011 0904567

Abstract

This work deals with the joining of porous Fe22Cr ferritic stainless steel to a dense Crofer22APU plate by using a silica-based, Ba-containing glass-ceramic. The chemical and interfacial stability and the mechanical properties of the joints were evaluated before and after thermal ageing at 700°C for 500hrs. The sintering behaviour of the glass was assessed by using heating stage microscopy (HSM) to study the influence of a porous metal substrate on the shrinkage of the joining material. Scanning electron microscopy revealed that there were no defects or cracks at the porous alloy/glass-ceramic interface for both the as-joined samples and the samples after thermal ageing at 700°C for 500 hrs. However, at this exposure temperature, the porous alloy started to form an oxide scale at the interface with the glass-ceramic and the internal surface of

the porous alloy. Finally, the evaluation of the mechanical properties by tensile testing showed that the properties were not affected by thermal ageing at 700°C.

Keywords: Glass-ceramics; joining; porous alloys; metal-supported SOC

1. Introduction

The porous metallic alloys sector is a major area of interest within the field of high-temperature engineering materials. The functional role of the porosity can be exploited in catalytic reactors (thanks to the high surface area for reactions), filters and metal-supported solid oxide cells (MS-SOCs).

Previous studies have evaluated the oxidation resistance of these alloys in the dense form [1–4] and they have been used for many decades as MS-SOCs [5], but recent studies on high-temperature corrosion of porous metal alloys [6–9] led to increasing interest due to important engineering features such as open porosity which allows gas transport and therefore these materials can be used for gas permeation membranes. Therefore, porous ferritic stainless steels (FSSs) constitute suitable candidate materials for use as metallic interconnects with high-temperature ceramic fuel cells[9,10] and gas separation membranes [11–13].

Solid oxide cell (SOC) technology has been developed due to its higher efficiency compared to combustion engines, silent operation and fast charging. Improvements in materials, cell design and manufacturing processing have led to a very high level of technical refinement. More recently, due to the tendency of the cell to fail and assembling issues associated with the use of complex ceramic parts, there has been interest in alternative MS-SOC which can be exploited in the temperature range of 650-

800°C [14] thanks to their low cost, flexibility, robustness and manufacturability benefits. MS-SOCs allow for a lower cost balance of plant components (BoP) and higher redox stability.

To choose the most suitable material to produce interconnects, it is desirable to match the coefficient of thermal expansion (CTE) of the metal to that of the electrolyte[15]. Most manufacturers prefer Fe and Cr-based materials as ferritic stainless steels (e.g. 430 alloy), which are commonly used for automotive exhaust manifolds and mufflers thanks to their inexpensive and high-temperature resistance. This is the reason why FSSs have substituted the more expensive and difficult to manufacture ceramic interconnects in SOC design [16,17].

One of the major challenges in the design of solid oxide cell stacks is the selection of joining materials for sealing the metallic interconnect. The sealant role is fundamental to assure high durability and long-term performance. The most common sealing materials are glass-ceramics due to the simplicity of the sinter-crystallization process and the possibility to tailor their composition and thermo-mechanical properties. Moreover, several studies have reported that they can exhibit higher gas tightness than other typical sealants (i.e. brazing alloys) and superior stability in extreme working conditions [18–20]. Another advantage of using glass-ceramics is linked to the presence of a residual glassy phase after the sinter-crystallization process, which can minimize thermal stresses and provide self-healing properties that are very useful in thermal cycling conditions [21]. Furthermore, the formation of crystalline phases within the glass phase improves mechanical properties and drives the choice of the composition in terms of thermo-mechanical compatibility involving the coefficient of thermal expansion (CTE) matching with the SOC components[22].

The selected sealant inevitably influences the stability and the chemical compatibility at the interface between the sealant material and the SOC components. Some studies have shown that undesirable interfacial reactions are possible between Cr-based stainless steels and glass-ceramic sealants. For example, the $BaCrO_4$ phase that has a high CTE (~ 21-23 x 10^{-6} K^{-1}) can form at the interface between Ba-containing glass-ceramics and Cr-containing metal interconnects [20,23].

Despite this, many research groups have studied and demonstrated the affinity and the effectiveness of glass-based sealants in solid oxide cells [24–27] and many suitable BaO-SiO_2-Al_2O_3-based systems have been successfully developed for SOC applications [25,28], but the current state of the art associated to the joining of porous to bulk alloys in SOCs by glass-based materials is very limited [29].

Previous studies [30] carried out oxidation tests of mixed glass-ceramics with FSS powders and revealed decreased oxidation rate compared with raw steel powder and suggested that the resulting oxide scale can enhance the sealant properties.

However, very few studies have dealt with the oxidation processes of porous ferritic stainless steels and there has been no detailed investigation of the joining and integration issues of these materials. A systematic understanding of how the stainless-steel porosity and the consequent corrosion reactions affect the interfacial behaviour with glass-based materials is still lacking.

This study describes the joining of porous Fe22Cr alloy to a dense Crofer 22APU plate with a silica barium-based glass-ceramic. The interfacial behaviour between the silica barium-based glass-ceramic and both dense and porous alloy interconnects will be discussed with particular focus on the morphological and chemical characterisation at the interface before and after thermal ageing at 700°C for 500 h in air. Finally, tensile

tests were performed on joined samples, comparing the tensile strength and the fracture surface between as-joined and aged specimens.

2. Materials and methods

The Fe22Cr porous alloy substrate (of composition Cr = 22 wt.%; Mn = 0.23 wt.%; Si = 0.08 wt.%; Ni, Cu, Mo <0.03 wt.%, with Fe representing the balance), was produced by Höganäs AB (Höganäs, Sweden) and characterised for its resistance against high temperature oxidation in a study by Koszelow et al [9]. The ~0.4 mm thick porous sheet was manufactured by tape-casting of a steel particle slurry, followed by drying, debinding and sintering at 1250°C in a pure H_2 atmosphere for 30 minutes. Dense steel coupons were cut from a 0.3-mm-thick plate of Crofer22APU (Cr = 23 wt.%, Mn = 0.45 wt.%, La = 0.1 wt.%, Ti = 0.06 wt.%, Si and Al < 0.05 wt.% with Fe representing the balance) provided by VDM Metals (Verdohl, Germany). Both porous and dense substrates were cleaned in acetone and ethanol for 10 min each in an ultrasonic bath. The joining material was a Ba-based glass-ceramic, referred to as GC2 [31]. The original glass was produced using conventional melting and casting from the following high-purity grade raw materials: SiO_2 (Sigma Aldrich, 99.5 % purity) with 55 mol%, B_2O_3(precursor H_3BO_3, Sigma Aldrich, 99% purity) with 8 mol%, Al_2O_3 (Alfa Aesar, 99.9 % purity) with 4 mol%, CaO (precursor $CaCO_3$ Sigma Aldrich, 99 % purity) with 7 mol % and BaO (precursor Ba_2CO_3 Thermoscientific, 99.8 % purity) with 26 mol%. All the raw material powders were mixed for 24 hrs and melted in a Pt-Rh crucible in an electric furnace (LHT418PN2, Nabertherm GmbH, Lilienthal/ Bremen, Germany) in air at 1500 °C for 1 h (the first 30 minutes a lid covered the crucible). The melt was cast onto a metal plate and the glass was subsequently ball-milled and sieved (particle

size < 38 μm). The sintering behaviour of the glass powders on the porous substrate, as well as on Al_2O_3 inert substrate was investigated using heating stage microscopy (HSM; Hesse Heating Microscope, Germany), with a heating rate of 5°C/min, from room temperature up to the melting point identified by the instrument.

A small quantity of a slurry paste composed of ethanol (70 wt.%) and glass powder (30 wt.%) was manually deposited with a spatula between the two metal alloys (squared specimens ~11 mm X ~11 mm) to be joined. Preliminary tests carried out with different configurations led to the most effective joint with pre-oxidised (900°C, 2h as dwelling time, at a 5°C/min as heating/cooling rate) dense Crofer22APU placed on the top. The joining process was carried out in air at 950°C for 1h (5°C/min as heating/cooling rate) in a muffle furnace (L5/13/P330, Nabertherm GmbH, Lilienthal/ Bremen, Germany). During the heat treatment, a stainless-steel weight was placed on top of the sandwich structure to apply a pressure of around 1.5 kPa. A Computed Tomography (CT) scan (Fraunhofer IKTS, Hermsdorf, Germany) was used to obtain morphological and qualitative density information of the joined sample under the following parameters: 9.25 μm as resolution, 280kV as acceleration voltage and 1s the exposure time for each projection. The reconstruction of the joint consists of creating a 3D model of the analysed volume by the CT software.

The same heat treatment identified for the joined sample was also used to produce a dry pressed glass-ceramic pellet, using uniaxial pressure of 12 MPa, to thermo-mechanically characterise GC2 glass-ceramic. The coefficient of thermal expansion (CTE) and the dilatometric softening point of as-cast GC2 glass and as-joined glass-ceramic were measured using a dilatometer (Netzsch, DIL 402 PC) equipped with an

alumina sample holder, at a heating rate of 5°C/min, applying a constant compressive force, between the sample and the piston of 0.25N.

Some joined samples were cross-sectioned and prepared for SEM and EDS analyses, while others were subjected to ageing treatment at 700°C for 500 hrs in a muffle furnace (Carbolite Gero, Hope Valley, UK). This temperature was chosen based on the results obtained by Koszelow et al. [9] focused on the corrosion study of the same Fe22Cr porous alloy up to 900°C. Some joint samples underwent tensile testing before and after thermal ageing using a method modified from the ASTM C633-01 standard. The tests were carried out using a Syntech 10/D machine (MTS Systems Corporation, Minnesota, USA). Each joint was adhered to two loading fixtures (Figure 1) by using Araldite® 2015 epoxy resin and thermally treated at 85°C for 1h to crosslink. The cross-head speed was set to 0.5 mm/min. The tensile strength was calculated by dividing the maximum force by the area of the joint which measured 11 mm x 11 mm. A field-emission scanning electron microscope (FESEM; SupraTM 40, Zeiss, Oberkochen, Germany) equipped with an energy dispersive X-ray analyser (EDS, Bruker, Germany) was used to characterise the morphology of the samples, which were previously polished using SiC papers (grit size 600-4000) and coated with Cr. A benchtop scanning electron microscope (SEM, JCM-6000 plus, Jeol, Peabody, Massachusetts, USA) was used to observe the fractured surface of the samples following mechanical testing. X-ray diffraction (XRD) analysis of the fractured surface of a joined sample after ageing was conducted using an X'Pert Pro MRD diffractometer, with Cu Kα radiation (PANalytical X'Pert Pro, Philips, Almelo, The Netherlands), and with the aid of X-Pert HighScore software, while the phases were identified using the JCPDS database

provided by PDF-4 ICDD (International Centre for Diffraction Data, Newton Square, Pennsylvania, the USA).

Figure 1. Configuration used for the mechanical tensile test.

3. Results and Discussion

Figure 2 reports the experimental curves obtained from heating stage microscopy (HSM) analyses of the as-cast GC2 glass powder pellets on the porous Fe22Cr alloy (curve 1) and on an inert Al_2O_3 support (curve 2), where the linear shrinkages % are plotted against the temperature. The first two characteristic temperatures are the points at which linear shrinkage of the glass starts (T_{fs}) and assumes the maximum value (T_{ms}): they are 705°C and 790°C on the porous alloy, 696°C and 802°C on the Al_2O_3 substrate. The temperature at which the first signs of softening are observed (DT) was identified at 811°C (onto Fe22Cr) and 822°C (onto Al_2O_3) , while the sphere temperature (ST) was at 893°C on the porous alloy and 872°C on Al_2O_3, where the height of the sample is equal to the width of the base. The half-sphere temperature (HT), which is the temperature at which the height of the sample is half the width of the base, was measured at 1028°C on the Fe22Cr porous alloy and at 1040°C on the inert substrate. Finally, the flow temperature (FT) was evident at 1079°C and 1076°C; the latter is the temperature at which the height of the sample drops to below one-third of the base. A visible plateau between 800 and 1000°C was observed and this represents the crystallization phenomenon that occurs. A significant expansion of the glass powder pellet is visible for the GC2 glass onto the Fe22Cr porous alloy, which is evidently absent on the inert substrate; this is likely due to gaseous species developed at T higher than 920°C, determined by the oxidation of the porous alloy during the GC2 viscous flow sintering. Based on these observations, the conditions for joining the

porous samples to the bulk alloys were determined to be a temperature of 950°C with a dwelling time of 1h in air. This sinter-crystallization heat treatment led to the formation of GC2 glass-ceramic with $BaSi_2O_5$ as crystalline phase (CTE ~ 12.5 x 10^{-6} K^{-1}), obtained by the partial devitrification of the GC2 parent glass [32].

Figure 2. Heating Stage Microscopy (HSM) curves of the GC2 glass (5°C/min heating rate) on the Fe22Cr porous alloy (curve 1) and on the inert Al_2O_3 support (curve 2); characteristic temperatures of GC2 glass identified with HSM are shown below the figure.

In order to evaluate the thermo-mechanical properties of the microstructure obtained with the above-mentioned joining thermal treatment, dilatometry was used to measure the coefficient of thermal expansion (CTE) of the GC2 glass-ceramic as well as that of the parent glass (Figure 3). The CTE value of the GC2 as-cast glass is 9.2 x 10^{-6} K^{-1} between 200-500°C, while the glass transition temperature (T_g) and the dilatometric softening point are 665°C and 688°C respectively (Figure 3, curve 1). It can be observed from the dilatometric analysis of the GC2 glass-ceramic that T_g is slightly lower (658°C) with respect to the original glass and within experimental error, while the softening point is the same. However, there was evidence of an increase in the coefficient of thermal expansion of the glass-ceramic (10.7 x 10^{-6} K^{-1}) in comparison with that of the GC2 glass as suggested by the change in the slope of the curve (Figure 3, curve 2). The transformation of the parent glass into a glass ceramic led to a significant improvement of the CTE in the view of the thermomechanical compatibility of the final joined structure, since the CTEs of both the substrates to be joined (Crofer22APU and Fe22Cr) are around 11 x 10^{-6} K^{-1} (200-700°C).

Figure 3. Dilatometric curves of the GC2 as-cast glass (curve 1) and GC2 glass-ceramic obtained after sinter-crystallization at 950°C for 1h (curve 2); 5°C/min heating rate.

The sandwiched samples were processed, using the procedure described in the experimental section.

As observed in Figure 4 a, the SEM image of the cross-section of the joined sample showed excellent adhesion of the GC2 glass-ceramic with both the porous and dense metal alloys. No cracks or delamination are visible at the glass-ceramic/substrates interface resulting in a continuous joint along the entire length of the interface. Furthermore, there was no evidence of any reactions taking place by the interaction between the Crofer22APU/porous alloy and the glass (Figure 4 b,c) ; an average joint thickness of 520 μm was obtained using a pressure of 1.5 kPa. The presence of a few closed pores, homogeneously distributed in the glass-ceramic, could probably be due to the manual slurry method used to produce the joined specimens. On the other side, the larger voids observed only at the Fe22Cr porous alloy/GC2 glass-ceramic interface is probably due to gaseous species released from the porous substrate during sintering which occurred by viscous flow. Further SEM investigation carried out on a Crofer22APU/GC2 glass-ceramic/Crofer22APU joint (not reported here), showed the absence of these such big voids at both dense alloy/glass-ceramic interfaces, thus confirming that the bigger porosity is due only to the presence of the Fe22Cr porous alloy.

Figure 4. SEM images of the cross-section of (a) Crofer22APU/GC2 glass-ceramic/Fe22Cr porous alloy, (b) Crofer22APU/GC2 glass-ceramic interface (back-scattered) and (c) GC2 glass-ceramic/Fe22Cr porous alloy interface (back-scattered) obtained after sinter-crystallization at 950°C for 1h.

Most of the porosity was concentrated at the porous alloy/GC2 glass-ceramic interface as evidenced by SEM as well as computed tomography (CT) that was carried out on a joined sandwich-like specimen (Figure 5). In Figure 5a, a reconstructed 3D model of the sample is shown, while in the other images (Figure 5 b-d), 3 cross-sections are represented at a different distance from the porous alloy surface; these scans were taken close to the Fe22Cr/GC2 glass-ceramic interface (Figure 5b), in the middle of the joining area (Figure 5c) and finally further from the interface with the porous alloy. It is evident that most voids are located at the Fe22Cr/GC2 glass-ceramic interface, while in the other sections very few pores are shown.

Figure 5. CT-scan of a Crofer22APU/GC2 glass-ceramic/Fe22Cr porous alloy joined sample thermally treated at 950°C for 1 h. (a) 3D-model; sectioning plane (b) close to the porous alloy, (c) in the middle of the glass-ceramic, (d) close to Crofer22APU. The big pore on the right could be due to the manual slurry method used to produce the joined specimen.

More details concerning the Fe22Cr porous alloy/GC2 glass-ceramic interface are shown in FE-SEM images on a cross-sectioned joined sample in Figure 6. Close inspection at the interface shows that, despite the presence of pores that are concentrated in the lower part of the joining area, no cracks are located both in the joining area and at the interface. Strong adhesion between the GC2 glass-ceramic and the porous substrate can be observed (Figure 6a). The distribution of the crystalline phases produces a dense network of needle-like interlocked crystallites embedded in the residual glassy phase. EDS analysis in Figure 6d (spectrum 1) revealed the presence of Ba, Si and O, indicating the crystallization of a $BaSi_2O_5$ crystalline phase, homogeneously dispersed within the darker glassy matrix which reasonably shows a higher level of Al and Ca and a lower content of Ba and Si (spectrum 2); this hypothesis was supported by XRD

diffraction pattern of GC2 glass-ceramic after joining heat treatment at 950°C, 1h in air, as reported by Smeacetto et al. [32]. As shown in Figure 6c and the corresponding EDS in Figure 6d (spectrum 3), the glass infiltrates the porous alloy very well during the sinter-crystallization treatment; infiltration distance levels of up to 50 µm from the GC2 glass-ceramic/Fe22Cr porous alloy interface are evident.

Figure 6. Cross-section FE-SEM images at lower (a) and higher (b) magnification of the Fe22Cr porous alloy/GC2 glass-ceramic interface after sinter-crystallization at 950°C for 1h; (c) infiltration of the glass-ceramic in the porous alloy of the joined sample; (d) EDS analyses of the GC2 glass-ceramic in the joining area.

Tensile testing was used to evaluate the mechanical properties of the joined samples. The tests carried out on as-joined Crofer22APU/GC2 glass-ceramic/Fe22Cr porous alloy samples showed an average tensile strength of 7.4 ± 0.5 MPa (identified with σ_m in Figure 7). This value is slightly higher than the tensile strength of the majority of glass-ceramic sealants reported in the literature (3.8-6.3 MPa) and used for joining Crofer22APU and Crofer22H [33].

Figure 7. Macrographs of as-joined and aged Crofer22APU/GC2glass-ceramic/ Fe22Cr samples after tensile testing.

Macrographs of the fracture surface of 3 as-joined specimens are shown in Figure 7. While most of the fractured area of the Fe22Cr porous substrate in Figure 7 seems to show exposed metal alloy, however, EDS analyses (not reported here) revealed many parts of the surface covered by the GC2 glass-ceramic; in some areas, large sections (in white) of the GC2 glass-ceramic suggest the presence of cohesive failure, while small white specks show evidence of fractured glass-ceramic that had impregnated the pores of the Fe22Cr substrate. Inspection of the opposite part shows small fractured black

specks of Fe22Cr embedded in the GC2 glass-ceramic. These observations suggest that the impregnation of the glass-ceramic into the Fe22Cr porous alloy enhances the interfacial strength. Indeed, part of the failure seems to be occurring in the porous Fe22Cr just beyond the area of GC2 impregnation due to stress concentration in the porous alloy (due to the absence of GC2 glass-ceramic). Overall there is mixed adhesive/cohesive failure, where the adhesive failure is mainly localised at the porous/GC2 interface. Figure 8a shows a magnified fracture surface of the glass-ceramic on the Crofer22APU side after mechanical testing; the bright phase well visible in the back-scattered SEM image identified by the EDS analysis as $BaCrO_4$, was mainly located on the edges of the joined area and was present on both the porous and the dense metal alloy.

Figure 8. SEM images of top views of fracture surface of an as-joined (a) and an aged (b) Crofer22APU/GC2glass-ceramic/ Fe22Cr porous alloy sample after mechanical testing (Crofer22APU side); EDS analyses carried out on the fracture surfaces in the joining area.

Figure 9 shows a cross-section of a joined sample after ageing at 700°C for 500 hrs. There was no evidence of cracks following ageing, thus implying that detrimental thermal stresses did not occur. In addition, the microstructure of the GC2 glass-ceramic did not seem to be affected by the heat treatment (Figure 9a). However, Figure 9b shows evidence of the formation of an oxidation scale on the pores surface; oxidation was also apparent at the GC2 glass-ceramic/porous alloy interface (Figure 9c). Due to the large surface/volume ratio of the porous samples, there is a risk that oxide formation (typically Cr_2O_3 [34]) can potentially lead to depletion of Cr within the porous alloy. In a previously cited work [9], the surface of the same porous alloy, which was exposed to a temperature of 700°C for 100hrs, did not show any significant microstructural changes

in comparison to alloy samples that had not been aged. The weight gain at 700°C after 100 hrs was reported to be around 1%. However, a sample that had been exposed to 750°C for the same time, experienced a weight gain of ~2.5 % and was characterised by changes at the surface; a small amount of oxide had clearly formed at the surface which exhibited signs of greater roughness which may have resulted by the fact that the surface of the porous alloy was slightly rough. From Figure 9d the formation of a darker layer covering the Fe22Cr porous alloy following ageing is apparent. Based on the results of the EDS analysis the scale seems to be composed of a mixed Fe and Cr-based oxide and, since the latter is visible also further from the glass-ceramic/Fe22Cr porous alloy interface, it could be due to a longer ageing heat treatment (700°C for 500hrs).

Figure 9. FE-SEM images of a cross-section after ageing at 700°C for 500hrs: (a,c) Fe22Cr porous alloy/GC2 glass-ceramic interface and (b) Fe22Cr porous alloy; (d) higher magnification of Fe22Cr porous alloy and EDS analysis carried out on the porosity edge of the porous alloy.

The results of mechanical testing for the thermally-aged samples exhibited an average tensile strength of 7.7 ± 2.9 MPa, a value that was similar to the as-joined samples. Inspection of the macrographs in Figure 7 shows that the samples suffered a completely or mainly adhesive failure. Figure 8b shows a higher magnification of the fracture surface of the Crofer22APU after ageing at 700°C for 500 hrs following mechanical testing. The EDS analysis showed high atomic% of Ba and Cr and therefore the presence of barium chromate can be hypothesized also after ageing .

XRD analysis that was carried out on the Crofer22APU side (on the porous side, the remaining glass-ceramic layer was not enough) after ageing and mechanical testing, is shown in Figure 10. The main peaks matched with those of the orthorhombic barium

silicate (Sanbornite with chemical formula $BaSi_2O_5$, PDF card n. 01-071-1441), which was the main phase present after ageing. Prior to the ageing treatment, the only phase that was present was $BaSi_2O_5$ as previously reported for the as joined glass-ceramic system before ageing heat treatment [32]. However, following ageing, new phases emerged like those reported in previous studies with similar glasses [25], where the formation of additional Ba-Ca-silicate phases that were not homogeneously distributed within the microstructure was observed. In the present work a secondary phase identified as the barium calcium boron silicate (named Itsiite[35], crystal system: tetragonal; space group: I-42m) $Ba_2CaSi_4B_2O_{14}$, with PDF card n. 04-021-1159 was found. In addition, some low-intensity peaks were identified as the $BaCrO_4$ phase, confirming the EDS analyses carried out at the same fracture surface. Finally, the three peaks at about 2Θ=22.8°, 2Θ = 30.2° and 2Θ=34.5° could likely be attributed to $BaAl_2Si_2O_8$ (ref. code 00-012-0725). In the present work, the glass-ceramic joining material was subjected to a thermal ageing temperature that was 40°C higher than the GC2 glass-ceramic Tg value. These findings, while preliminary, suggest that this system is prone to further devitrification at temperatures slightly above the Tg. Despite this, the mechanical behaviour of the joints is not affected by this microstructural rearrangement. Further research should be undertaken to investigate the thermomechanical behaviour at temperatures higher than 700°C.

Figure 10. XRD pattern of the fracture surface (Crofer22APU side) of a Fe22Cr/GC2 glass-ceramic/Crofer22APU joined sample after ageing at 700°C for 500 hrs.

4. Conclusions

The possibility of using porous metal alloys provides interesting engineering features thanks to their functional porosity, which make these candidate materials for metal-supported solid oxide cells. The development of a dense to a porous joint can play a key role in the manufacture of reliable, efficient and durable metal-supported SOCs. The novelty of this study concerns the joining of porous stainless steel to a dense one with a glass-ceramic obtained from sinter-crystallization of a glass sealant. Different aspects concerning the interfacial issues and mechanical properties were discussed, evaluating an optimal adhesion and mechanical stability in Crofer22APU/GC2 glass-ceramic/ Fe22Cr porous alloy joints, before and after thermal ageing carried out at 700°C for 500hrs. The morphological analysis found no defects or cracks at the porous alloy/glass-ceramic interface, neither in the as-joined samples nor in samples after ageing at 700°C for 500 hrs. However, at this temperature, the porous alloy started to experience the formation of an oxidation scale at the interface between the Fe22Cr porous alloy and the GC2 glass-ceramic, as well as around the wall of the pores of the porous alloy. The mechanical strength of the joined samples was not affected by thermal ageing (7.4 MPa±0.5 before and 7.7 MPa ±2.9 after ageing).

The current study provides the first assessment concerning the joining of a porous to a dense alloy using glass-ceramics and makes the groundwork for future research into MS-SOC development.

Acknowledgments

DK and SM acknowledge the support of National Science Centre Poland (NCN) Sonata Bis 8 project number 2018/30/E/ST8/00821 “High-temperature corrosion studies

and development of oxidation lifetime model of alloy powders and sintered porous alloys: effects of composition and microstructure".

Declaration of competing interest

The authors declare that they have no known competing financial interests or personal relationships that could have appeared to influence the work reported in this paper.

References

[1] J.E. Hammer, S.J. Laney, R.W. Jackson, K. Coyne, F.S. Pettit, G.H. Meier, The oxidation of ferritic stainless steels in simulated solid-oxide fuel-cell atmospheres, Oxid. Met. 67 (2007) 1–38. https://doi.org/10.1007/s11085-006-9041-y.

[2] N.J. Magdefrau, L. Chen, E.Y. Sun, M. Aindow, Effects of alloy heat treatment on oxidation kinetics and scale morphology for crofer 22 APU, J. Power Sources. 241 (2013) 756–767. https://doi.org/10.1016/j.jpowsour.2013.03.181.

[3] P. Alnegren, M. Sattari, J. Froitzheim, J.E. Svensson, Degradation of ferritic stainless steels under conditions used for solid oxide fuel cells and electrolyzers at varying oxygen pressures, Corros. Sci. 110 (2016) 200–212. https://doi.org/10.1016/j.corsci.2016.04.030.

[4] B. Timurkutluk, S. Toros, S. Onbilgin, H.G. Korkmaz, Determination of formability characteristics of Crofer 22 APU sheets as interconnector for solid oxide fuel cells, Int. J. Hydrogen Energy. 43 (2018) 14638–14647. https://doi.org/10.1016/j.ijhydene.2018.04.243.

[5] S. Fontana, R. Amendola, S. Chevalier, P. Piccardo, G. Caboche, M. Viviani, R. Molins, M. Sennour, Metallic interconnects for SOFC: Characterisation of

corrosion resistance and conductivity evaluation at operating temperature of differently coated alloys, J. Power Sources. 171 (2007) 652–662. https://doi.org/10.1016/j.jpowsour.2007.06.255.

[6] D.N. Boccaccini, H.L. Frandsen, B.R. Sudireddy, P. Blennow, H. Persson, K. Kwok, P. Vang Hendriksen, Creep behaviour of porous metal supports for solid oxide fuel cells, Int. J. Hydrogen Energy. 39 (2014) 21569–21580. https://doi.org/10.1016/j.ijhydene.2014.07.138.

[7] M. Stange, C. Denonville, Y. Larring, A. Brevet, A. Montani, O. Sicardy, J. Mougin, P.O. Larsson, Improvement of corrosion properties of porous alloy supports for solid oxide fuel cells, Int. J. Hydrogen Energy. 42 (2017) 12485–12495. https://doi.org/10.1016/j.ijhydene.2017.03.170.

[8] E. Stefan, C. Denonville, Y. Larring, M. Stange, R. Haugsrud, Oxidation study of porous metal substrates for metal supported proton ceramic electrolyzer cells, Corros. Sci. 164 (2020) 108335. https://doi.org/10.1016/j.corsci.2019.108335.

[9] D. Koszelow, M. Makowska, F. Marone, J. Karczewski, P. Jasiński, S. Molin, High temperature corrosion evaluation and lifetime prediction of porous Fe22Cr stainless steel in air in temperature range 700–900 °C, Corros. Sci. 189 (2021). https://doi.org/10.1016/j.corsci.2021.109589.

[10] V. Venkatachalam, S. Molin, M. Chen, I. Smirnov, P.O. Larsson, P. V. Hendriksen, N. Bonanos, Optimization of ferritic steel porous supports for protonic fuel cells working at 600°C, Mater. Sci. Technol. Conf. Exhib. 2014, MS T 2014. 2 (2014) 1231–1239.

[11] Y. Xing, S. Baumann, D. Sebold, M. Rüttinger, A. Venskutonis, W.A. Meulenberg, D. Stöver, Chemical compatibility investigation of thin-film oxygen

transport membranes on metallic substrates, J. Am. Ceram. Soc. 94 (2011) 861–866. https://doi.org/10.1111/j.1551-2916.2010.04171.x.

[12] J.A. Calles, R. Sanz, D. Alique, Influence of the type of siliceous material used as intermediate layer in the preparation of hydrogen selective palladium composite membranes over a porous stainless steel support, Int. J. Hydrogen Energy. 37 (2012) 6030–6042. https://doi.org/10.1016/j.ijhydene.2011.12.164.

[13] J.A. Glasscock, L. Mikkelsen, Å.H. Persson, G. Pećanac, J. Malzbender, P. Blennow, F. Bozza, P. V. Hendriksen, Porous Fe21Cr7Al1Mo0.5Y metal supports for oxygen transport membranes: Thermo-mechanical properties, sintering and corrosion behaviour, Solid State Ionics. 242 (2013) 33–44. https://doi.org/10.1016/j.ssi.2013.04.006.

[14] S. Linderoth, Solid oxide cell R&D at Risø National Laboratory-and its transfer to technology, J. Electroceramics. 22 (2009) 61–66. https://doi.org/10.1007/s10832-008-9458-6.

[15] M.C. Tucker, Progress in metal-supported solid oxide fuel cells: A review, J. Power Sources. 195 (2010) 4570–4582. https://doi.org/10.1016/j.jpowsour.2010.02.035.

[16] M.C. Tucker, G.Y. Lau, C.P. Jacobson, L.C. DeJonghe, S.J. Visco, Stability and robustness of metal-supported SOFCs, J. Power Sources. 175 (2008) 447–451. https://doi.org/10.1016/j.jpowsour.2007.09.032.

[17] M.C. Tucker, Durability of symmetric-structured metal-supported solid oxide fuel cells, J. Power Sources. 369 (2017) 6–12. https://doi.org/10.1016/j.jpowsour.2017.09.075.

[18] J.W. Fergus, Sealants for solid oxide fuel cells, J. Power Sources. 147 (2005) 46–

57. https://doi.org/10.1016/j.jpowsour.2005.05.002.

[19] M.K. Mahapatra, K. Lu, Seal glass for solid oxide fuel cells, J. Power Sources. 195 (2010) 7129–7139. https://doi.org/10.1016/j.jpowsour.2010.06.003.

[20] N. Mahato, A. Banerjee, A. Gupta, S. Omar, K. Balani, Progress in material selection for solid oxide fuel cell technology: A review, Prog. Mater. Sci. 72 (2015) 141–337. https://doi.org/10.1016/j.pmatsci.2015.01.001.

[21] R.N. Singh, Sealing Technology for Solid Oxide Fuel Cells (SOFC), Int. J. Appl. Ceram. Technol. 4 (2007) 134–144. https://doi.org/10.1111/j.1744-7402.2007.02128.x.

[22] F. Smeacetto, A. De Miranda, A. Chrysanthou, E. Bernardo, M. Secco, M. Bindi, M. Salvo, A.G. Sabato, M. Ferraris, Novel glass-ceramic composition as sealant for SOFCs, J. Am. Ceram. Soc. 97 (2014) 3835–3842. https://doi.org/10.1111/jace.13219.

[23] M.K. Mahapatra, K. Lu, Glass-based seals for solid oxide fuel and electrolyzer cells - A review, Mater. Sci. Eng. R Reports. 67 (2010) 65–85. https://doi.org/10.1016/j.mser.2009.12.002.

[24] S.M. Gross, T. Koppitz, J. Remmel, J.B. Bouche, U. Reisgen, Joining properties of a composite glass-ceramic sealant, Fuel Cells Bull. 2006 (2006) 12–15. https://doi.org/10.1016/S1464-2859(06)71320-7.

[25] J. Schilm, A. Rost, M. Kusnezoff, S. Megel, A. Michaelis, Glass ceramics sealants for SOFC interconnects based on a high chromium sinter alloy, Int. J. Appl. Ceram. Technol. 15 (2018) 239–254. https://doi.org/10.1111/ijac.12811.

[26] H. Javed, A.G. Sabato, K. Herbrig, D. Ferrero, C. Walter, M. Salvo, F. Smeacetto, Design and characterization of novel glass-ceramic sealants for solid oxide

electrolysis cell (SOEC) applications, Int. J. Appl. Ceram. Technol. 15 (2018) 999–1010. https://doi.org/10.1111/ijac.12889.

[27] A.G. Sabato, A. Chrysanthou, M. Salvo, G. Cempura, F. Smeacetto, Interface stability between bare, Mn–Co spinel coated AISI 441 stainless steel and a diopside-based glass-ceramic sealant, Int. J. Hydrogen Energy. 43 (2018) 1824–1834. https://doi.org/10.1016/j.ijhydene.2017.11.150.

[28] J. Schilm, A. Rost, M. Kusnezoff, A. Michaelis, Sealing Glasses for SOFC - Degradation Behaviour, in: Adv. Solid Oxide Fuel Cells V, 2010: pp. 183–193. https://doi.org/10.1002/9780470584316.ch17.

[29] D. Udomsilp, J. Rechberger, R. Neubauer, C. Bischof, F. Thaler, W. Schafbauer, N.H. Menzler, L.G.J. de Haart, A. Nenning, A.K. Opitz, O. Guillon, M. Bram, Metal-Supported Solid Oxide Fuel Cells with Exceptionally High Power Density for Range Extender Systems, Cell Reports Phys. Sci. 1 (2020). https://doi.org/10.1016/j.xcrp.2020.100072.

[30] A. Drewniak, D. Koszelow, P. Błaszczak, K. Górnicka, K. Jurak, H. Javed, A.G. Sabato, P. Jasiński, S. Molin, F. Smeacetto, Glass-ceramic sealants and steel interconnects: Accelerated interfacial stability and reactivity tests at high temperature, Mater. Des. 212 (2021). https://doi.org/10.1016/j.matdes.2021.110259.

[31] M. Ferraris, S. De la Pierre, A.G. Sabato, F. Smeacetto, H. Javed, C. Walter, J. Malzbender, Torsional shear strength behavior of advanced glass-ceramic sealants for SOFC/SOEC applications, J. Eur. Ceram. Soc. 40 (2020) 4067–4075. https://doi.org/10.1016/j.jeurceramsoc.2020.04.034.

[32] F. Smeacetto, A. Chrysanthou, A.G. Sabato, H. Javed, S.D. la Pierre, M. Salvo, M.

Ferraris, Glass-to-metal seals for solid oxide cells at the Politecnico di Torino, an overview, Int. J. Appl. Ceram. Technol. 19 (2022) 1017–1028. https://doi.org/10.1111/ijac.13949.

[33] B. Cela Greven, S. Gross-Barsnick, T. Koppitz, R. Conradt, F. Smeacetto, A. Ventrella, M. Ferraris, Torsional shear strength of novel glass-ceramic composite sealants for solid oxide fuel cell stacks, Int. J. Appl. Ceram. Technol. 15 (2018) 286–295. https://doi.org/10.1111/ijac.12819.

[34] L. Wang, W. Yang, Z. Ma, J. Zhu, Y. Li, First-principles study of chromium di ff usion in the ferritic Fe-Cr alloy, Comput. Mater. Sci. 181 (2020) 109733. https://doi.org/10.1016/j.commatsci.2020.109733.

[35] A.R. Kampf, R.C. Peterson, B.R. Joy, Itsiite, $Ba_2Ca(BSi_2O_7)_2$, a new mineral species from Yukon, Canada: Description and crystal structure, Can. Mineral. 52 (2014) 401–407. https://doi.org/10.3749/canmin.52.3.401.

Figure captions

Figure 1. Configuration used for the mechanical tensile test.

Figure 2. Heating Stage Microscopy (HSM) curves of the GC2 glass (5°C/min heating rate) on the Fe22Cr porous alloy (curve 1) and on the inert Al_2O_3 support (curve 2); characteristic temperatures of GC2 glass identified with HSM are shown below the figure.

Figure 3. Dilatometric curves of the GC2 as-cast glass (curve 1) and GC2 glass-ceramic obtained after sinter-crystallization at 950°C for 1h (curve 2); 5°C/min heating rate.

Figure 4. SEM images of the cross-section of (a) Crofer22APU/GC2 glass-ceramic/Fe22Cr porous alloy, (b) Crofer22APU/GC2 glass-ceramic interface (back-scattered) and (c) GC2 glass-ceramic/Fe22Cr porous alloy interface (back-scattered) obtained after sinter-crystallization at 950°C for 1h.

Figure 5. CT-scan of a Crofer22APU/GC2 glass-ceramic/Fe22Cr porous alloy joined sample thermally treated at 950°C for 1 h. (a) 3D-model; sectioning plane (b) close to the porous alloy, (c) in the middle of the glass-ceramic, (d) close to Crofer22APU. The big pore on the right could probably be due to the manual slurry method used to produce the joined specimen.

Figure 6. Cross-section FE-SEM images at lower (a) and higher (b) magnification of the Fe22Cr porous alloy/GC2 glass-ceramic interface after sinter-crystallization at 950°C for 1h; (c) infiltration of the glass-ceramic in the porous alloy of the joined sample; (d) EDS analyses of the GC2 glass-ceramic in the joining area.

Figure 7. Macrographs of as-joined and aged Crofer22APU/GC2glass-ceramic/ Fe22Cr samples after tensile testing.

Figure 8. SEM images of top views of fracture surface of an as-joined (a) and an aged (b) Crofer22APU/GC2glass-ceramic/ Fe22Cr porous alloy sample after mechanical testing (Crofer22APU side); EDS analyses carried out on the fracture surfaces in the joining area.

Figure 9. FE-SEM images of a cross-section after ageing at 700°C for 500hrs: (a,c) Fe22Cr porous alloy/GC2 glass-ceramic interface and (b) Fe22Cr porous alloy; (d) higher magnification of Fe22Cr porous alloy and EDS analysis carried out on the porosity edge of the porous alloy.

Figure 10. XRD pattern of the fracture surface (Crofer22APU side) of a Fe22Cr/GC2 glass-ceramic/Crofer22APU joined sample after ageing at 700°C for 500 hrs.

Figure 1

Click here to access/download;Figure;fig1.jpg

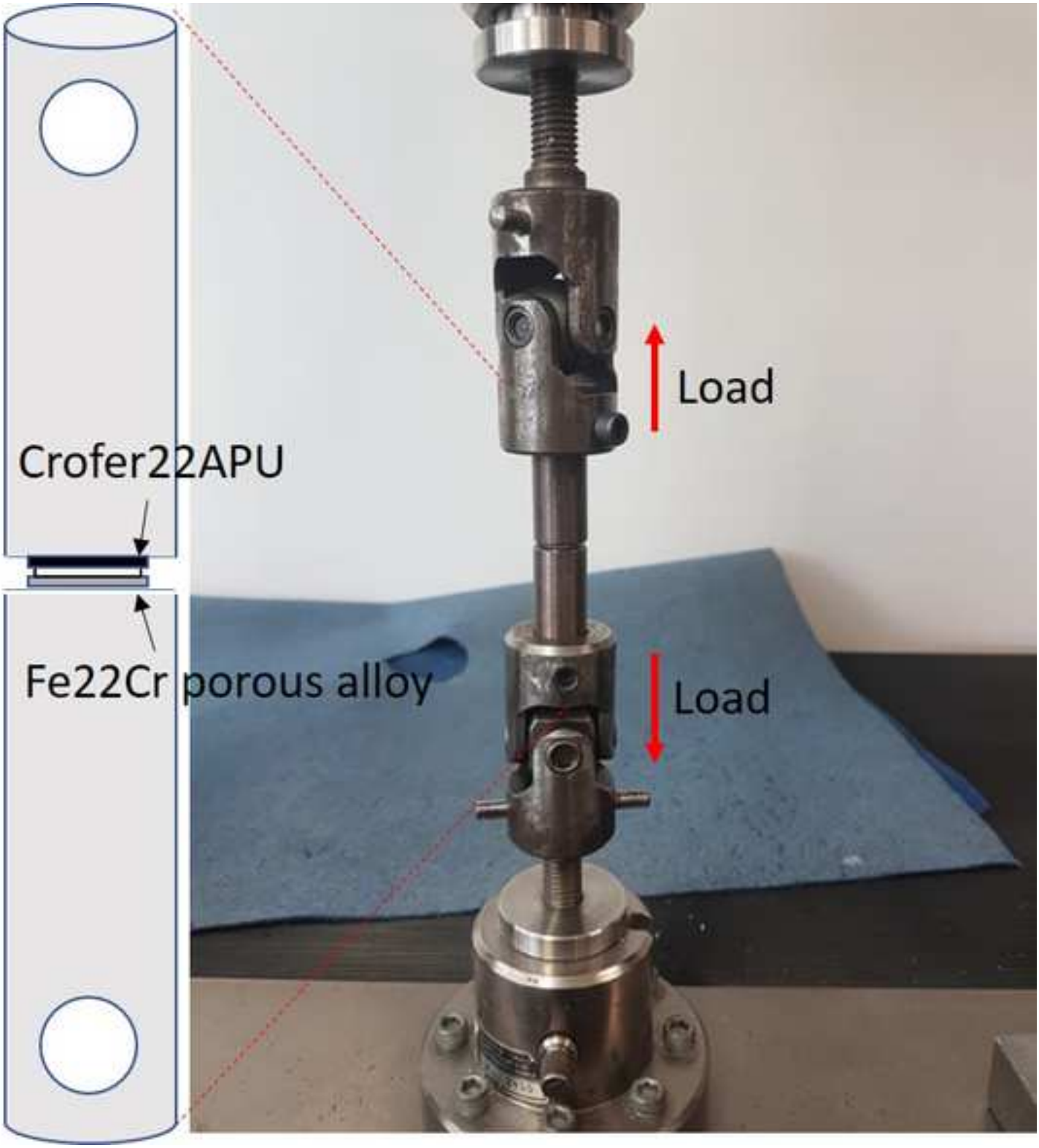


Figure 2

Click here to access/download;Figure;fig2.jpg

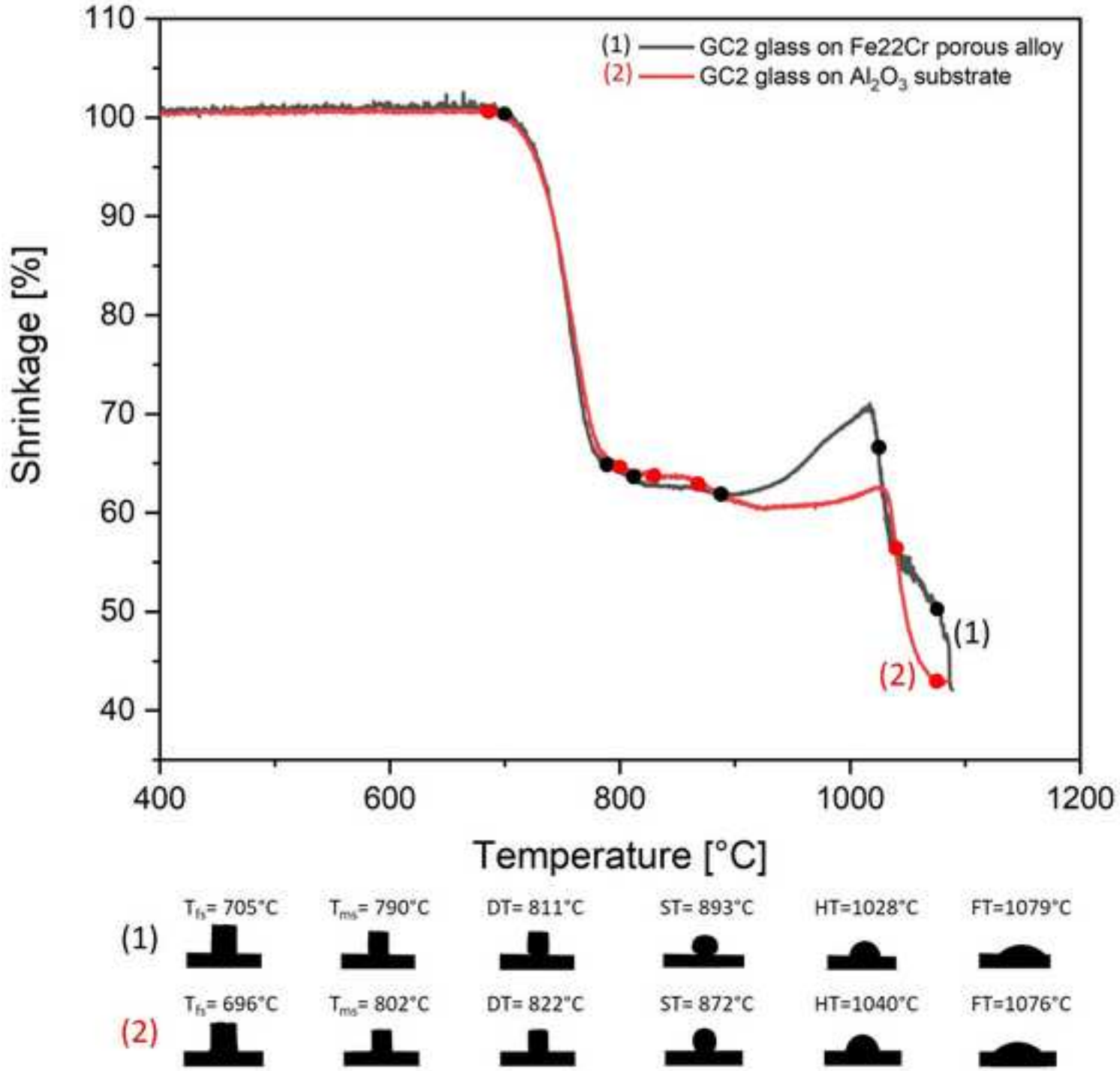


Figure 3

Click here to access/download;Figure;fig3.jpg

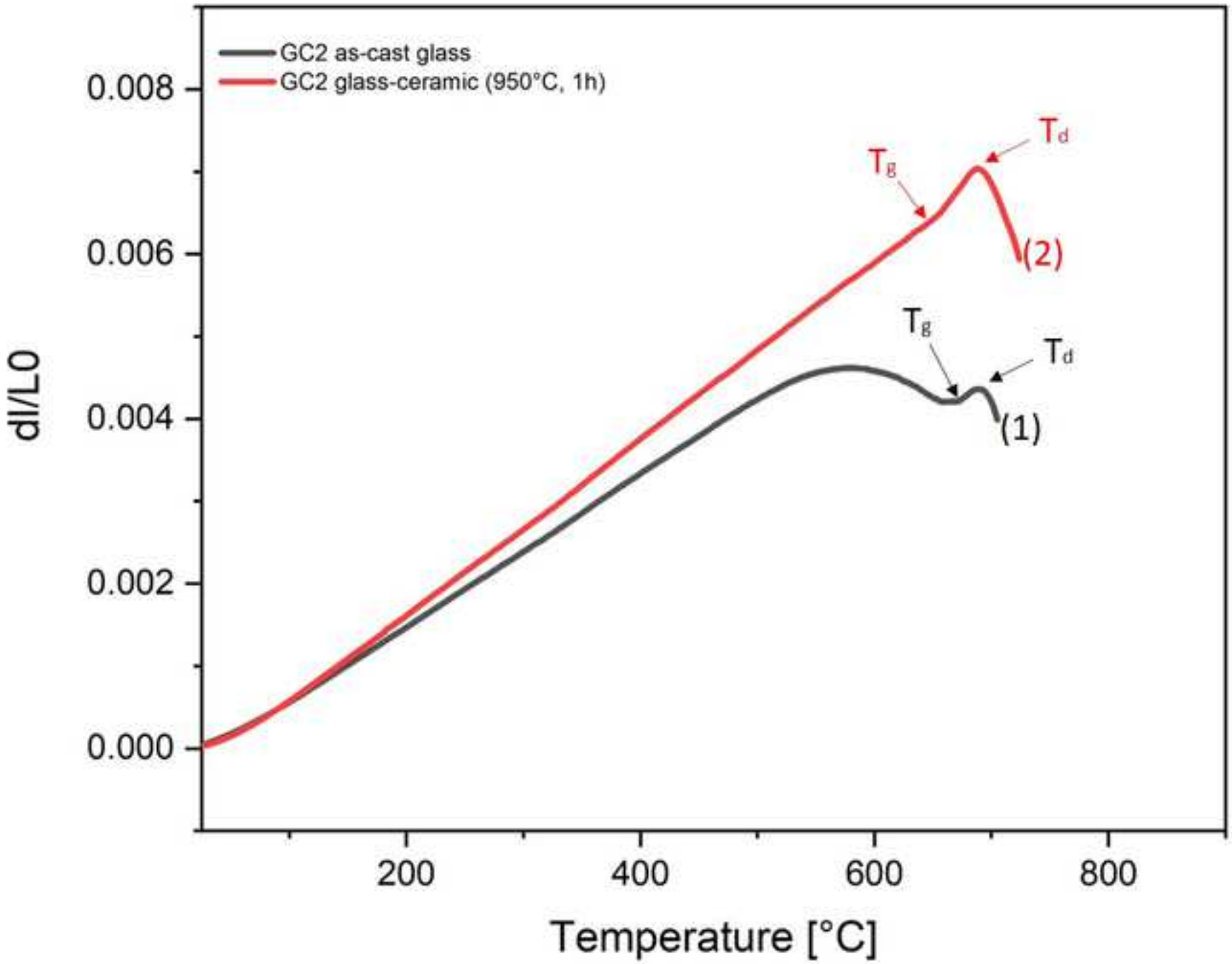


Figure 4

Click here to access/download;Figure;fig4.jpg

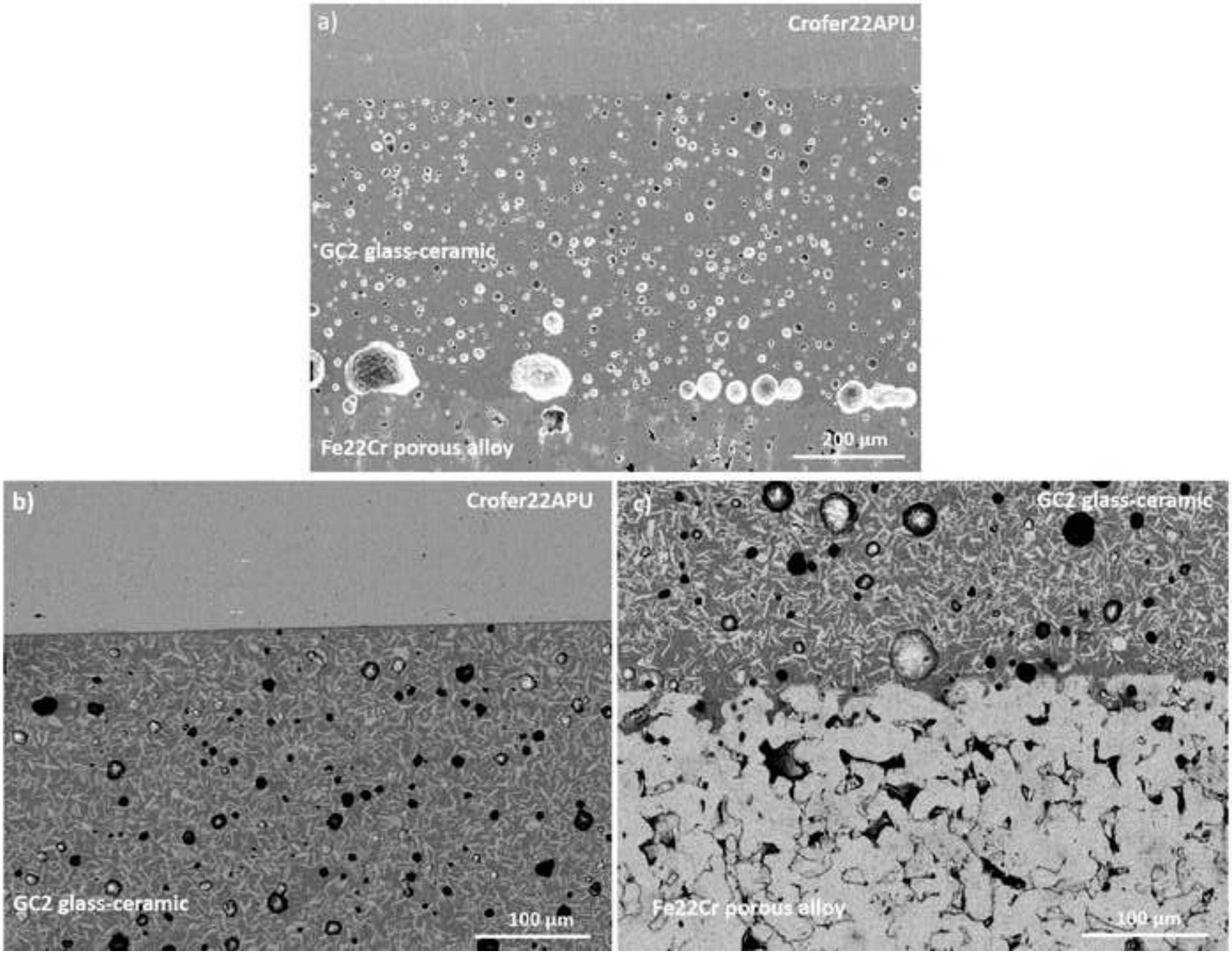


Figure 5

Click here to access/download;Figure;fig5.jpg

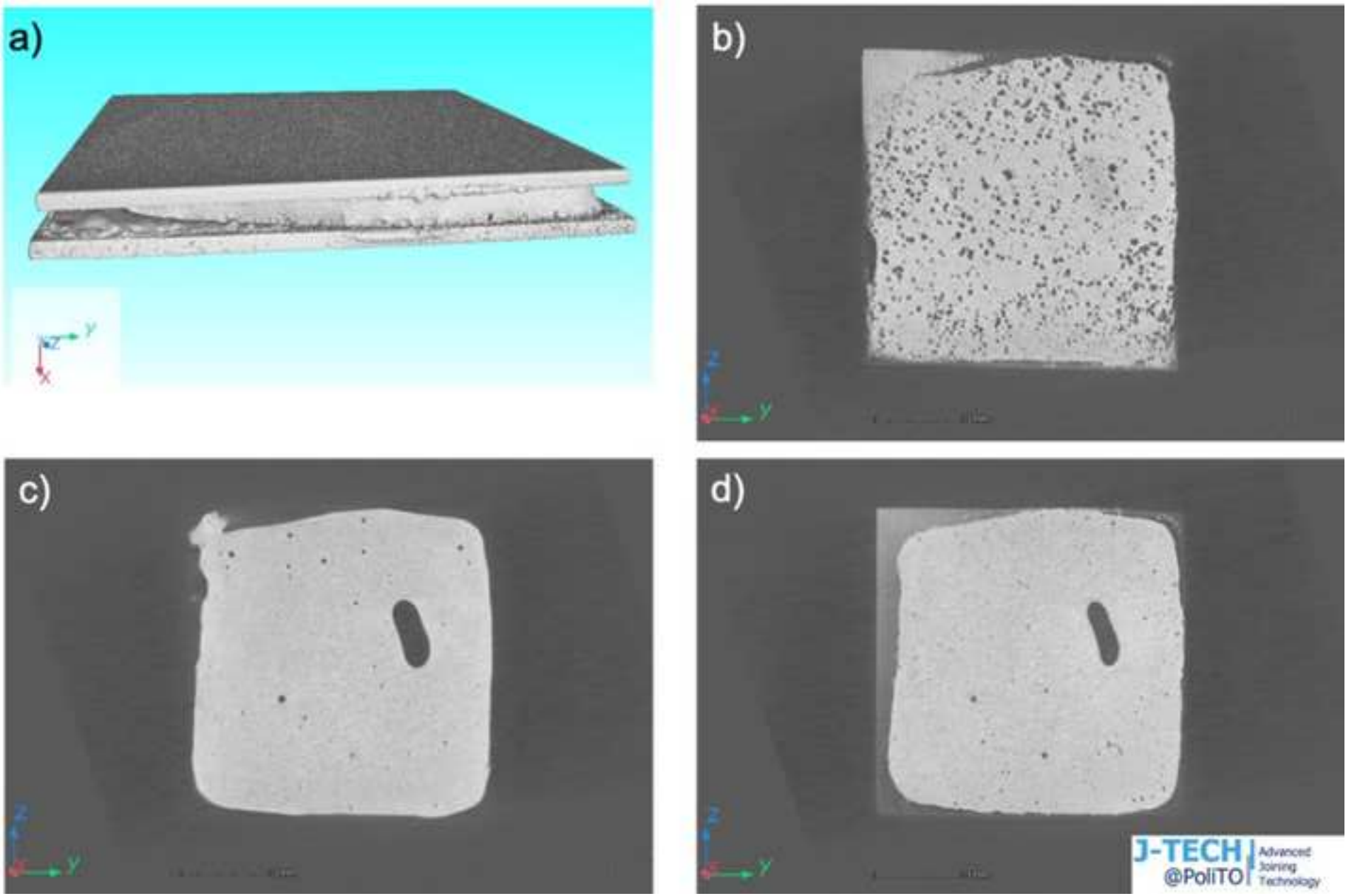
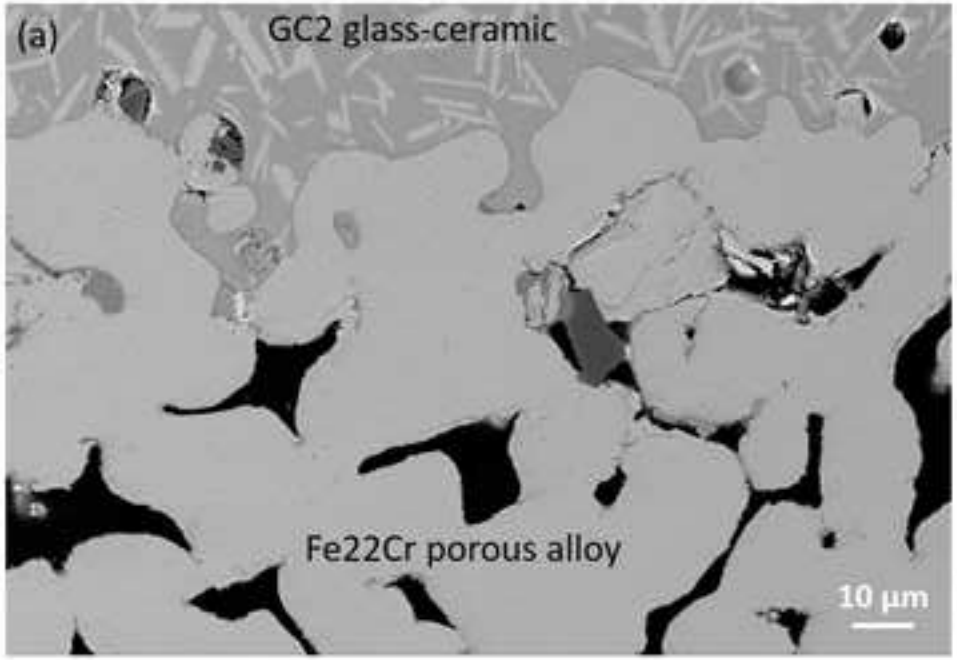
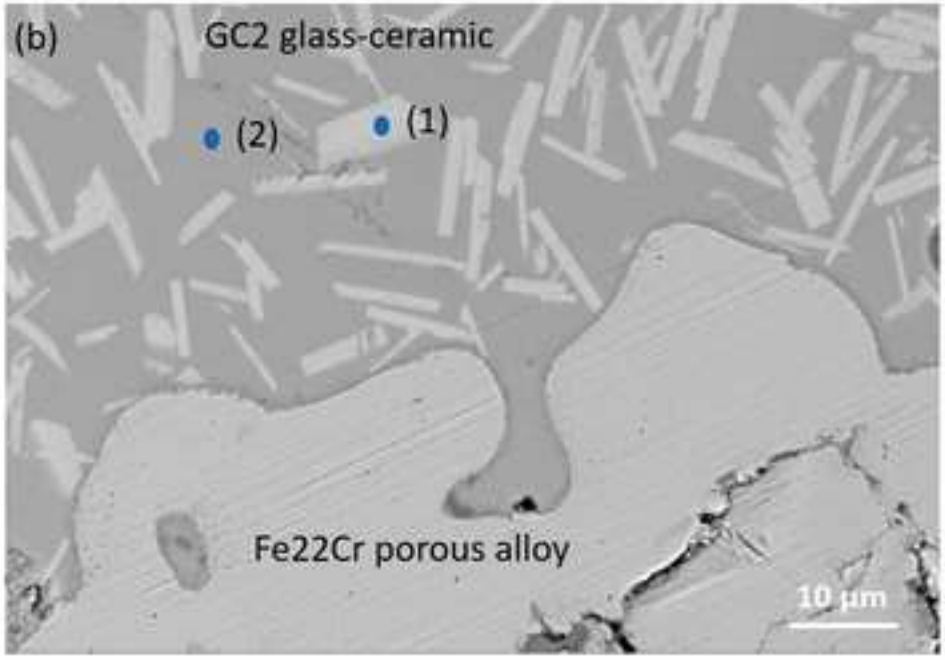
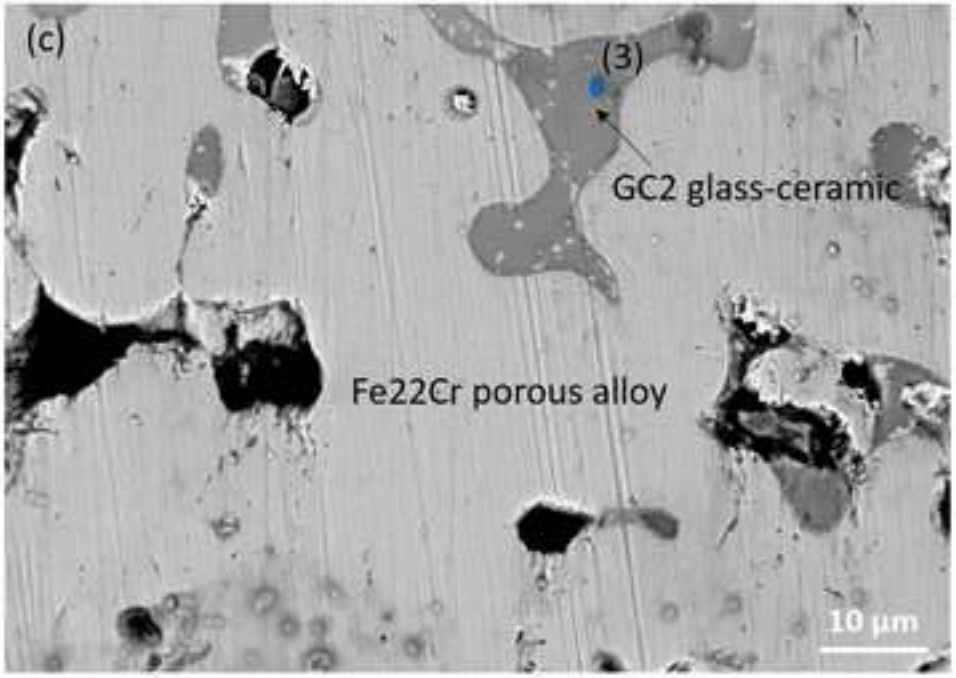


Figure 6

Click here to access/download;Figure;fig6.jpg







(d) Elements	(1) Atomic %	(2) Atomic %	(3) Atomic %
O	61.7	65.1	63.7
Al	1.0	3.5	3.3
Si	25.1	20.5	22.2
Ca	1.2	2.9	2.7
Ba	11.2	8.0	7.1
Fe	-	-	1.0
Tot	100.0	100.0	100.0

Figure 7

Click here to access/download;Figure;fig7.jpg

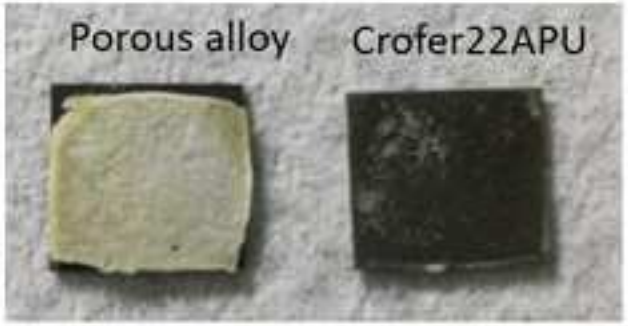
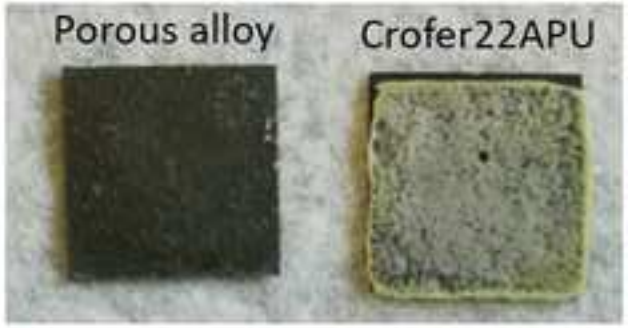
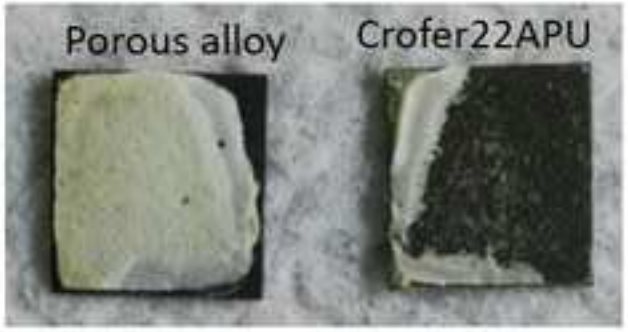
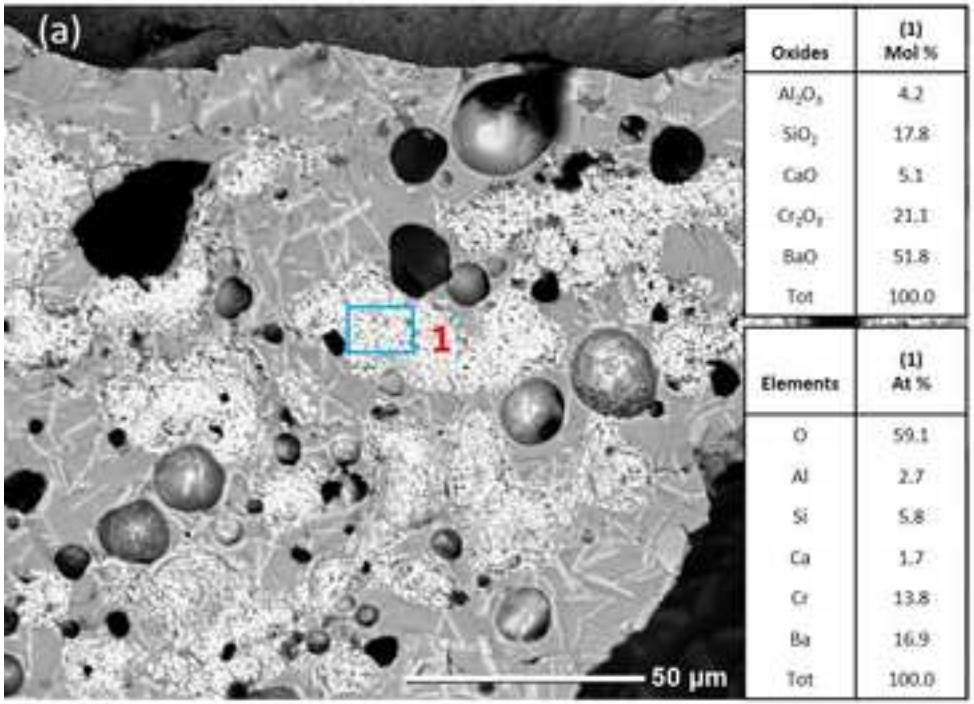
Samples	Before ageing	After ageing
n.1		
n.2		
n.3		
σ_m [MPa]	7.4 ± 0.5	7.7 ± 2.9

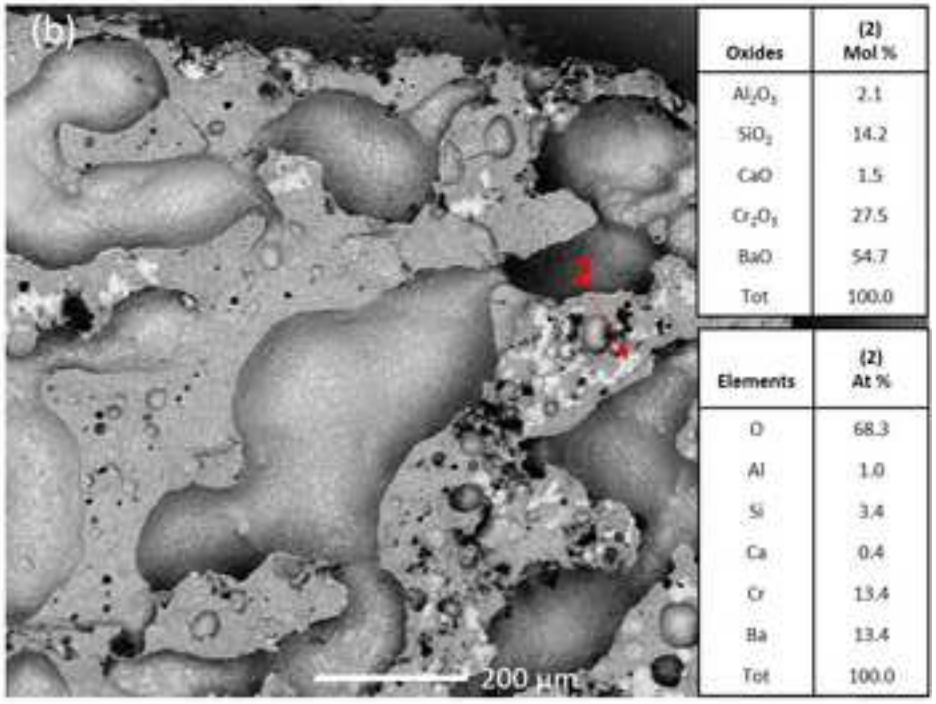
Figure 8_revised

Click here to access/download;Figure;Fig.8_rev.jpg



Oxides	(1) Mol %
Al_2O_3	4.2
SiO_2	17.8
CaO	5.1
Cr_2O_3	21.1
BaO	51.8
Tot	100.0

Elements	(1) At %
O	59.1
Al	2.7
Si	5.8
Ca	1.7
Cr	13.8
Ba	16.9
Tot	100.0

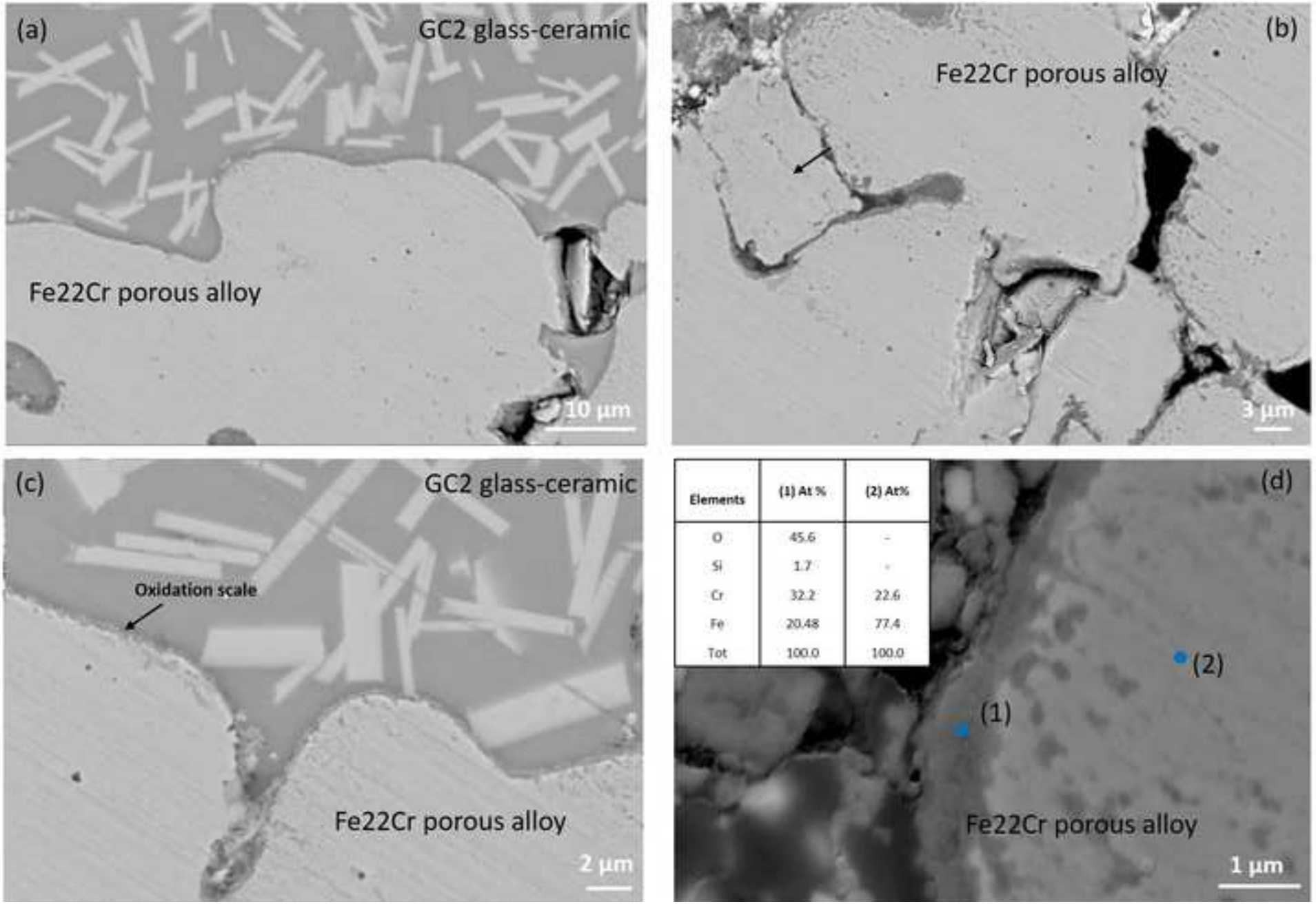


Oxides	(2) Mol %
Al_2O_3	2.1
SiO_2	14.2
CaO	1.5
Cr_2O_3	27.5
BaO	54.7
Tot	100.0

Elements	(2) At %
O	68.3
Al	1.0
Si	3.4
Ca	0.4
Cr	13.4
Ba	13.4
Tot	100.0

Figure 9

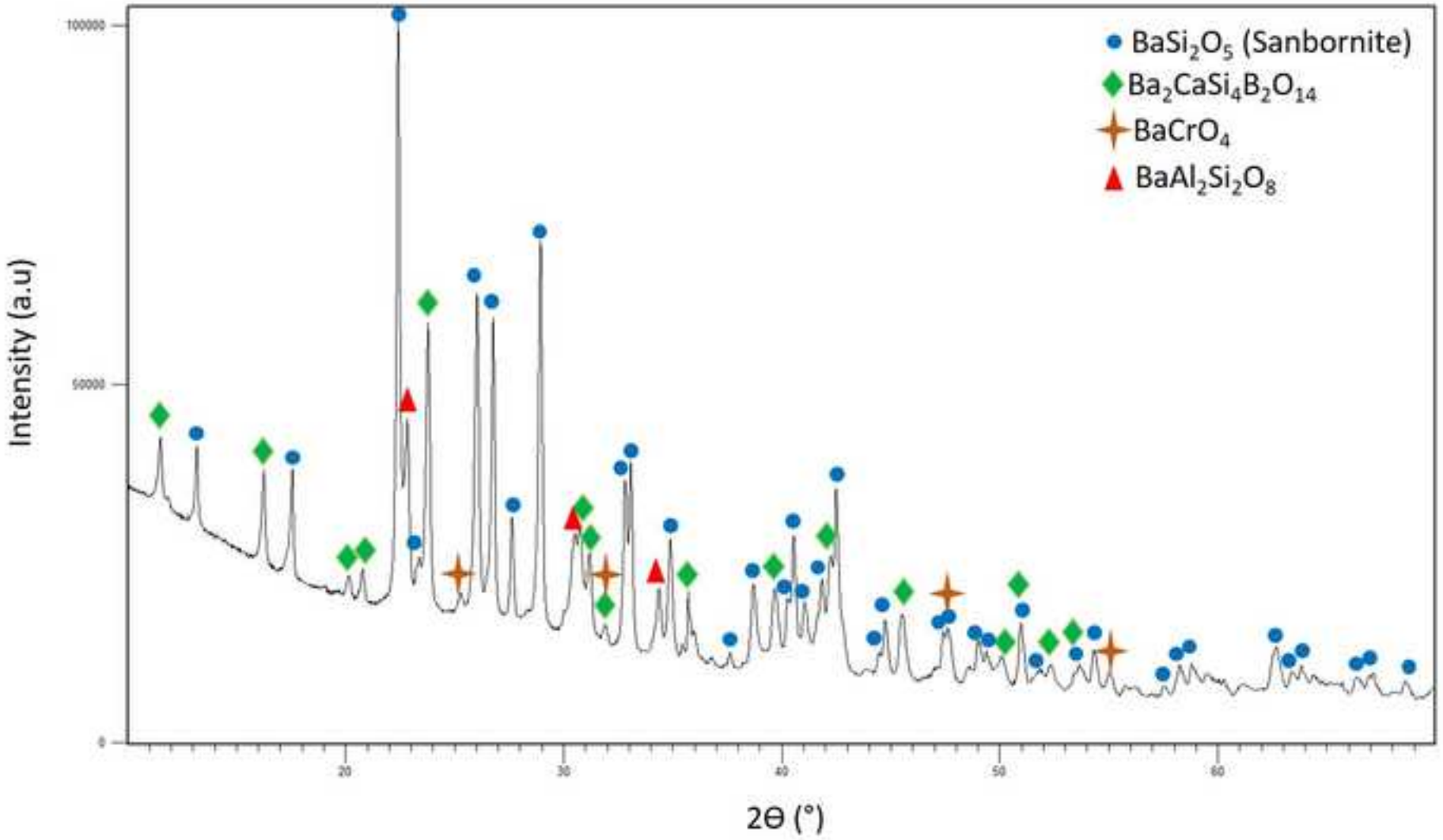
Click here to access/download;Figure;fig 9.jpg



Elements	(1) At %	(2) At%
O	45.6	-
Si	1.7	-
Cr	32.2	22.6
Fe	20.48	77.4
Tot	100.0	100.0

Figure 10_revised

Click here to access/download;Figure;Fig.10_rev.jpg



declaration of interest statement

Declaration of interests

☒ The authors declare that they have no known competing financial interests or personal relationships that could have appeared to influence the work reported in this paper.

☐The authors declare the following financial interests/personal relationships which may be considered as potential competing interests: